Analysis of Multivalley and Multibandgap Absorption and Enhancement of Free Carriers Related to Exciton Screening in Hybrid Perovskites

Jacky Even, Laurent Pedesseau, Claudine Katan

J. Phys. Chem. C, 2014, 118 (22), pp 11566–11572 DOI: 10.1021/jp503337a

Analysis of multi-valley and multi-bandgap absorption and enhancement of free carriers related to exciton screening in hybrid perovskites

Jacky Even,[†] Laurent Pedesseau,[†] and Claudine Katan*[‡]

[†]Université Européenne de Bretagne, INSA, FOTON, UMR 6082, 35708 Rennes, France

[‡]CNRS, Institut des Sciences Chimiques de Rennes, UMR 6226, 35042 Rennes, France

Corresponding Author

*Email: Jacky.Even@insa-rennes.fr Tel: +33 (0)2 23 23 82 95, Claudine.Katan@univ-rennes1.fr Tel: +33 (0)2 23 23 56 82

J. Phys. Chem. C, 2014, 118 (22), pp 11566–11572 DOI: 10.1021/jp503337a

Solution-processable metal-halide perovskites recently opened a new route towards low-cost manufacture of photovoltaic cells. Converting sunlight into electrical energy depends on several factors among which a broad absorption across the solar spectrum and attractive charge transport properties are of primary importance. Hybrid perovskites meet such prerequisites but, despite foremost experimental research efforts, their understanding remains scanty. Here we show that in these materials, the appropriate absorption and transport properties are afforded by the multi-bandgap and multi-valley nature of their band structure. We also investigate the nature of the photoexcited species. Our analysis suggests exciton screening by collective orientational motion of the organic cations at room temperature, leading to almost free carriers. Molecular collective motion is also expected to couple to carrier diffusion at room temperature. In mixed-halides, our interpretation indicates that doping might hinder collective molecular motions, leading to good transport properties despite alloying and local lattice strain.

TOC GRAPHICS

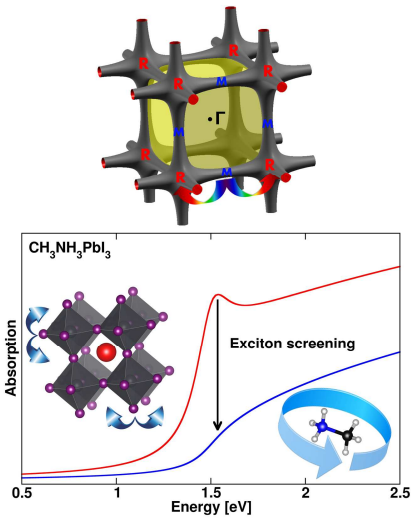

KEYWORDS Hybrid perovskites, solar cells, optoelectronics, density functional theory, exciton

J. Phys. Chem. C, 2014, 118 (22), pp 11566–11572 DOI: 10.1021/jp503337a

In a photovoltaic (PV) device, the conversion efficiency of solar radiation into electrical power is paramount. In 1961, Shockley and Queisser established the theoretical efficiency limit of an ideal single p-n junction solar cell, based on the principle of detailed balance.[1] This limit of 33.7% is almost attained by the best-performing heterojunctions[2]. Among the strategies developed to bypass this limit, concentrated multi-junction (multiple p-n junctions) PV cells[2,3] undeniably afford upmost conversion efficiencies[2] but at the expense of elaborate and expensive growth modus operandi. Conversely, solution-processable metal-halide perovskites have recently opened a new route towards low-cost manufacture of solar cells.[4-16] The tremendous research effort conducted during the last 2 years has mainly focused on the methylammonium lead-iodide perovskite ($CH_3NH_3PbX_3$, X=I). First used as the sensitizer in conventional dye sensitized solar cells[4-6], thanks to its good light harvesting abilities, its attractive charge transport properties allowed to achieve Meso-Superstructured Solar Cells (MSSC) and solid thin-film planar heterojunctions with record efficiencies up to 15%.[7-15] In fact, broad absorption across the solar spectrum and appropriate electron and/or hole mobilities are prerequisites to high solar-to-electrical power conversion efficiencies. While there is clear experimental evidence that lead-halide perovskites meet these conditions, the understanding of underlying mechanism remains scarce.[14-16] As Loi and Hummelen put forward, "*it is now time to investigate the physical properties that make hybrid perovskites so promising for solar-energy conversion*".[16] First, the origin of the favorable light absorption over the visible to near-IR range is still mysterious in spite of a couple of recent theoretical investigations.[17-23] At room temperature, the linear absorption spectrum of $CH_3NH_3PbI_3$ shows two absorption peaks located at 760 and 480 nm.[14-15] Whereas the low energy peak was attributed to the direct bandgap transition from the valence

J. Phys. Chem. C, 2014, 118 (22), pp 11566–11572 DOI: 10.1021/jp503337a

band (VB) maximum to the conduction band (CB) minimum, the origin of the high-energy peak is clearly unresolved.[15] Moreover, a hot hole cooling mechanism was also suggested for the intra-band relaxation after optical excitation at high energy for $CH_3NH_3PbI_3$.[15] Besides, halogen substitution ($X_3=I_{3-x}Cl_x$ or $I_{3-x}Br_x$) has shown to provide improved transport properties and cell stability while preserving good performances including low fundamental energy losses.[5,11-14] To understand such improvements, Snaith and colleagues have recently thoroughly investigated the carrier dynamics after optical excitation for $X_3=I_{3-x}Cl_x$.[24] It is shown that after photoexcitation the second order transient THz transmission dynamics of triiodide compounds is an order of magnitude faster than for the mixed halide. Moreover, the latter exhibit larger mobilities (+43%), sizeable enhancement of the absorption above the bandgap and a threefold increase of the photoluminescence radiative lifetime.[24] Snaith and colleagues suggest localization of electrons and holes in different regions of the perovskite's unit cell but do not rule out the presence of excitons in the material following photoexcitation.[24] Thus, it is still unclear whether the photoexcited species are excitons or free charges. Moreover, little is known about what could make mixed halides superior to triiodide perovskites, namely the origin of increased mobilities and decreased charge carrier recombinations that enhance PV efficiencies. We may also notice that the frequency-dependence of the dielectric constant has been highlighted in a very recent review paper.[25]

Here we report a theoretical investigation of a series of metal-halide perovskites: $CH_3NH_3PbX_3$, X=I, Br, Cl. First, we thoroughly analyse calculated absorption spectra of the reference cubic phase of lead-based compounds. Next, we discuss the nature of the photoexcited species based on extensive use and modeling of both recent and older experimental findings, namely temperature dependent absorption spectra,[26,27] millimeter-wave spectroscopy,[28] low

frequency dielectric measurements,[29] and NMR data related to the motion of molecular cations.[30] Then we discuss in sequence the impact of halogen substitution on absorption and carrier mobilities. Computational details are provided in the Supporting Information.

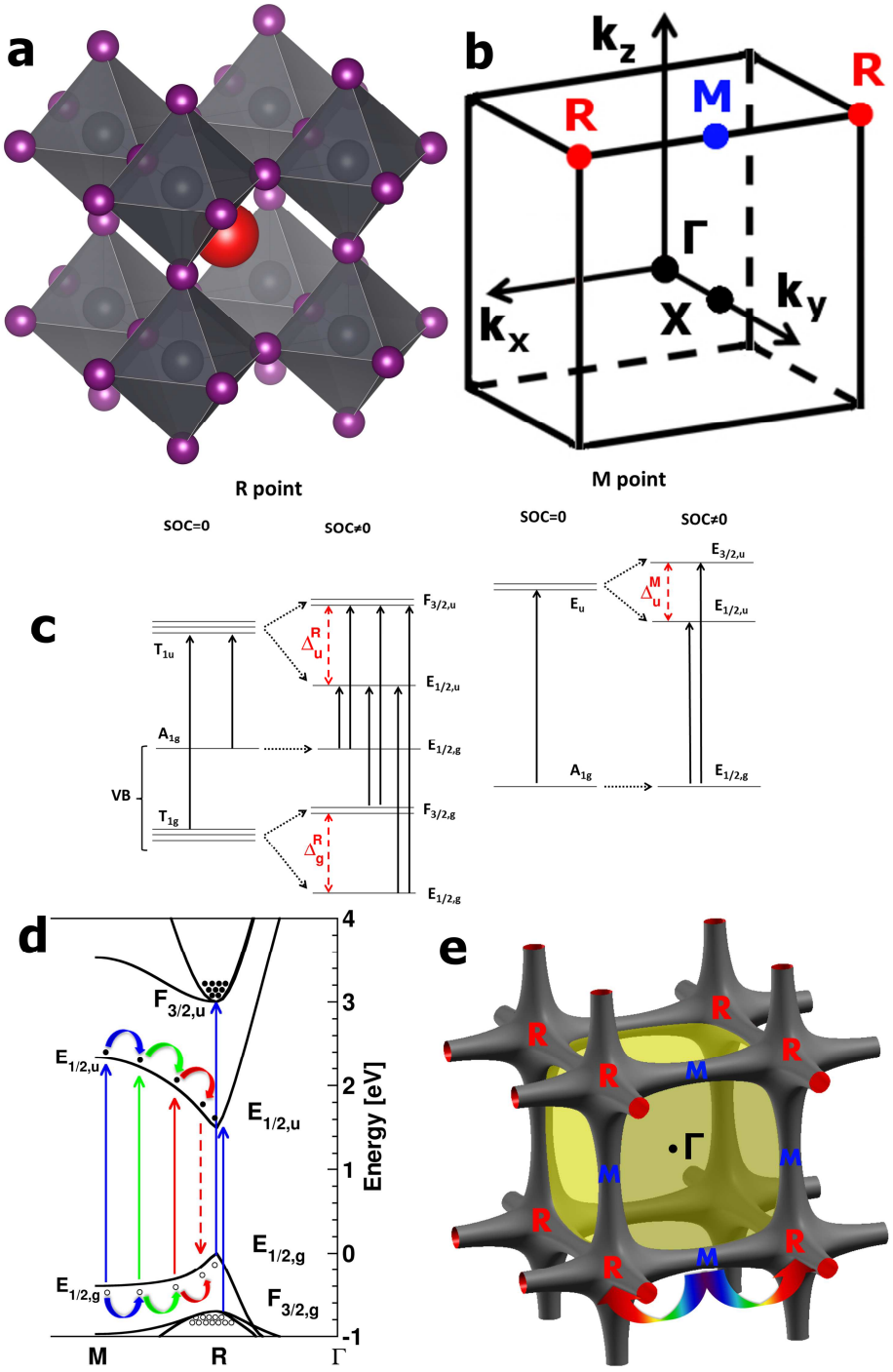

J. Phys. Chem. C, 2014, 118 (22), pp 11566–11572 DOI: 10.1021/jp503337a

Figure 1. Analysis of optical absorption spectra of $CH_3NH_3MX_3$ based on group theory, electronic band diagram and Fermi surface. **a**, Real space 3D view of the Pm3m cubic crystal structure of metal-halide hybrid perovskites of general formulae $CH_3NH_3MX_3$. The $CH_3NH_3^+$ cation is located at the center of the cube with an averaged position sketched by a red ball. **b**, Reciprocal space 3D view showing the first Brillouin Zone (BZ) of the Pm3m space group. Points of high symmetry in the cubic BZ are indicated by conventional letters: Γ denotes the origin of the BZ; X is the center of a square face at the BZ boundary, M is a center of a cube edge; and R are vertices of the cube. **c**, Schematic energy levels diagrams drawn at the high symmetry R and M points of the Pm3m BZ. Irreducible representations of the simple (SOC=0, where SOC denotes spin orbit coupling) and double (SOC≠0) groups are indicated. The level splitting associated to SOC are labeled Δ_g^R, Δ_u^R and Δ_u^M. The additional spin degeneracy is not indicated for the double group representations. The upward arrows show the symmetry allowed optical transitions. **d**, Electronic band diagram of the high temperature Pm3m cubic phase of $CH_3NH_3PbI_3$ taking SOC into account; an upward energy shift of 1.4eV has been applied to match the experimental bandgap value at R. Carrier localization and transport after optical excitation are sketched. **e**, Fermi surface (E=-0.5eV) in the first BZ. R and M are connected along the edges, highlighting the saddle point nature of M.

The ideal cubic crystal structure (Pm3m space group) of metal-halide perovskites is sketched Figure 1a together with the corresponding Brillouin Zone (BZ) in reciprocal space (Figure 1b). It has been shown that symmetry analysis of this ideal cubic phase is relevant for crystal structures having a group-subgroup relationship.[18] Thus the electronic band structure of the room temperature (RT) tetragonal phase of $CH_3NH_3PbI_3$ is directly connected to that of the cubic phase.[18] The latter has high symmetry points among which the R and M are of major importance

J. Phys. Chem. C, 2014, 118 (22), pp 11566–11572 DOI: 10.1021/jp503337a

to our purpose. In fact, recent calculations of the imaginary part of the dielectric function for the high temperature cubic phase of $CH_3NH_3PbI_3$, based on density functional theory (DFT) within the Random-Phase Approximation (RPA), evidenced the onsets of primary and secondary absorptions related to R and M points, respectively.[18] Similar features are obtained for $CH_3NH_3PbCl_3$ (Figure S4 in the Supporting Information). These calculations do not consider spin-orbit coupling (SOC) that induces giant splittings of the CB of lead-based hybrid perovskites.[17,18,32] A first insight in these optical features can be gained from group theory. The symmetry analysis of the electronic states at R and M in the simple (without SOC) and double (with SOC) group allows identifying the optically allowed transitions. The simple group T_{1u} vectorial representation of the CB at R is splitted in a doubly degenerated $E_{1/2u}$ (spin-orbit split-off states) and a fourfold degenerated $F_{3/2u}$ state (Figure 1c). The ground state isotropic optical transition is thus predicted at R between doubly degenerated $E_{1/2g}$ VB and $E_{1/2u}$ CB states depicted Figure 1d for the calculated band structure. Complete diagrams with and without SOC are provided in Figure S1 and S2 (Supporting Information). At R, a series of other transitions are optically allowed, the lowest in energy corresponding to two secondary transitions $F_{3/2g} \rightarrow E_{1/2u}$ and $E_{1/2g} \rightarrow F_{3/2u}$ (Figure 1). The transition between the doubly degenerated $E_{1/2g}$ VB and $E_{1/2u}$ CB states at M is also optically allowed and transverse electric (TE). To determine which of these transitions is responsible for the peak experimentally observed at 480nm in the absorption spectra, we evaluate the strength of the optical transitions, as defined by optical matrix elements (Table S2 and S3 in the Supporting Information). Values are significantly larger for M, thanks to a threefold contribution, and the upwards 1eV energy shift is consistent with experimental findings. The threefold contribution can be intuited from the Fermi surface plotted in the first BZ close to the top of the VB (Figure 1e). Moreover, the different optically allowed transitions have

sizeable matrix elements disclosing the multi-bandgap nature at the origin of broad absorption of $CH_3NH_3PbI_3$, expanding from the visible to the near-IR (see also in the Supporting Information).

Next, the Fermi surface (isoenergy surface below the valence band maximum at -0.5eV, Figure 1e) reveals clear connection between R and M along the edges of the BZ. While the BZ valleys are located around R, M correspond to saddle points. This suggests that, in reciprocal space, hole carriers generated by optical absorption at M and all along the M→R paths at various wavelengths (Figure 1d) can flow easily towards R. The relaxation process may be assisted by acoustic phonons or coupling to collective molecular rotations (vide infra). Contrarily, one expects that some of the carriers generated by the secondary optical transitions at R may be trapped in the $F_{3/2u}$ (CB) and $F_{3/2g}$ (VB) states (Figure 1d). Further relaxation $F_{3/2g} \rightarrow E_{1/2g}$ (holes) and $F_{3/2u} \rightarrow E_{1/2u}$ (electrons) may occur by optical phonons assisted relaxations, provided that the energy conservation rule is fulfilled. Such a "phonon bottleneck" is well known in the case of carrier injection in semiconductor quantum dots.[33-35] However, in quantum dots, carrier assisted (Auger relaxation) is the dominant effect in the high injection regime, yielding very fast carrier relaxation. A similar hot hole cooling (intra-band process) from $F_{3/2g}$ to $E_{1/2g}$ is consistent with the relaxation after optical excitation reported for $CH_3NH_3PbI_3$.[15] Similar results are obtained for the cubic Pm3m phase of $CH_3NH_3PbCl_3$ (Figure S3, Tables S4 and S5 in the Supporting Information), with a larger bandgap and a larger splitting between primary (R) and secondary (M) optical transitions.

Let's now discuss about the nature of the photoexcited species at room temperature. For the secondary transition at M, excitonic effects are expected to be small as a consequence of its saddle point nature (Figures 1d,e). This is consistent with the absence of excitonic features at higher energy in the spectrum recorded at 4.2 K.[26] If experimental studies clearly exhibit

J. Phys. Chem. C, 2014, 118 (22), pp 11566–11572 DOI: 10.1021/jp503337a

excitonic effects in the low-energy part of the absorption spectra of $CH_3NH_3PbX_3$ at low temperatures (LT),[26,36,37] the situation is less straightforward at RT. In fact, recent experiments performed at RT have been analysed considering free carrier transport.[24,38,39] For instance, achievement of planar heterojunction cells has been related to low bimolecular charge recombination constants suggesting spatial separation of opposite charge carriers within the perovskite.[24] Next, if the exciton binding energies reported at LT (37-50meV)[26,36,37] remain unchanged at RT ($kT \approx 26$ meV), free charge carriers and excitons should coexist.[24] To gauge the importance and origin of screening we may go back to experimental data recorded two decades ago. Ishihara et al. reported absorption spectra of $CH_3NH_3PbI_3$ at different temperatures.[27] These data are consistent with an exciton quenching between 159K and 212K (Figure 2), in relation with the structural transition at Tc=162K. The exciton quenching includes both exciton screening and gap-switching[17,18] (ill-named exciton-switching), that also appears in 2D hybrids[27,40] (see also in the Supporting Information). This prompts need for a better understanding of the exciton at RT.

J. Phys. Chem. C, 2014, 118 (22), pp 11566–11572 DOI: 10.1021/jp503337a

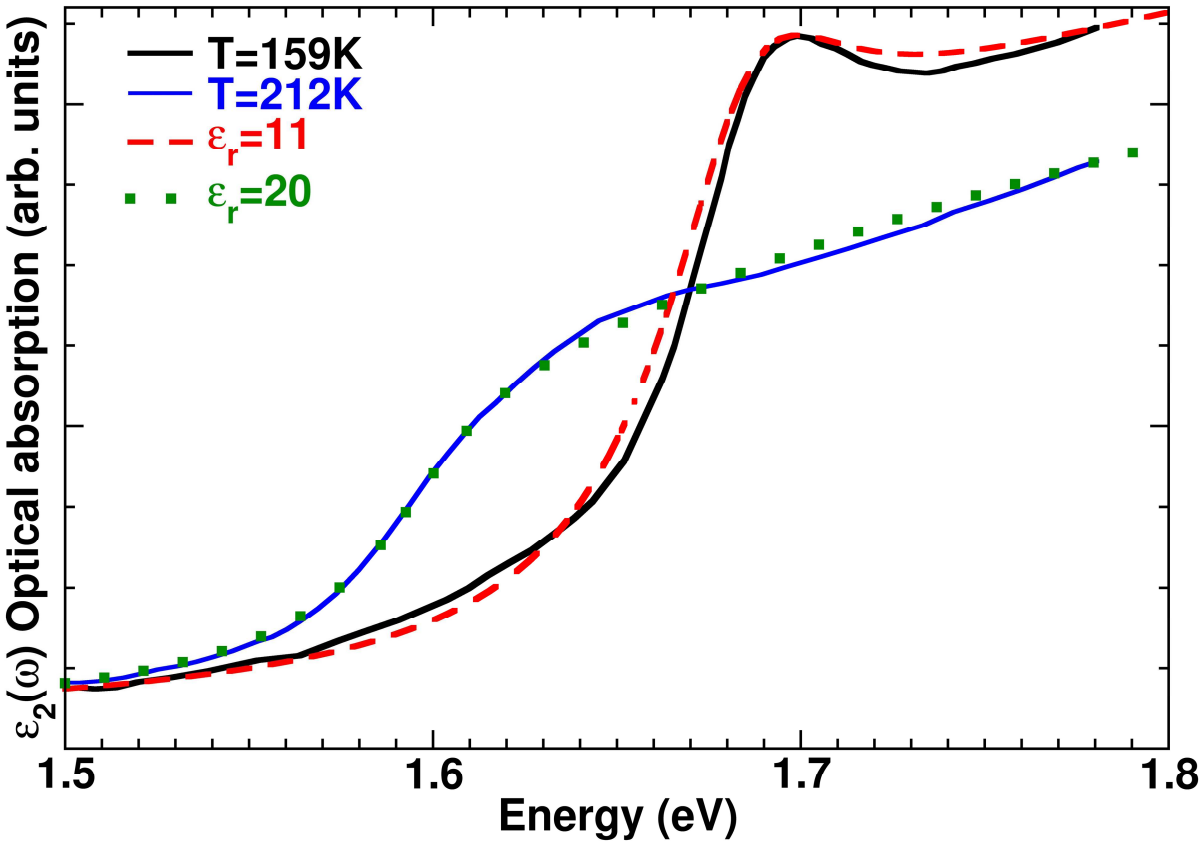

Figure 2. Optical absorption spectra of $CH_3NH_3PbI_3$ highlighting exciton screening. Experimental data taken from Ref. 27 recorded at 159 K (black line) and 212 K (blue line) and computed spectra for bound and continuum pair states, considering two-particle wave function and effective mass equations for electron and hole (expression (3) with $\gamma = 0.03eV$ and $\mu = 0.16m_e$). The effect of dielectric screening is shown for ε_{eff} =11 (red dash line) and 20 (green dot line) and leads to a good fit of the experimental spectra below (159K) and above Tc (212K), respectively.

Theoretically, excitonic effects can be accounted for using the Bethe-Salpeter Equation (BSE) starting from the monoelectronic states calculated at the DFT level. When taking the high temperature cubic phases of $CH_3NH_3PbCl_3$ (Figure S4 in the Supporting Information) and

$CH_3NH_3PbI_3$,[18] enhancement of absorption at the bandgap is clearly evidenced. But, in the perturbative BSE approach, screening of the electron-hole interaction due to atomic motion is not taken into account. This means that experimental results cannot be fully understood from BSE calculations, if the latter effects are important. A convenient way to simulate exciton screening is to consider a two-particle wave function $\psi(r_e, r_h)$, where r_e (r_h) is the electron (hole) position.[41] The effective mass approximation works well close to the bandgap in 3D hybrids both for electrons and holes,[18,23] thanks to the giant SOC in the CB leading to a non-degenerate band instead of a triply degenerate one obtained without SOC (vide infra).[17] For a Wannier exciton, the two-particle Hamiltonian including electrostatic interaction and effective mass approximation for electrons and holes reads: [41]

$$H = E_g - \frac{\hbar^2}{2m_e}\Delta_{re} - \frac{\hbar^2}{2m_h}\Delta_{rh} - \frac{e^2}{4\pi\varepsilon_{eff}|r_e - r_h|} \quad (1)$$

E_g is the bandgap energy, ε_{eff} the effective dielectric constant and m_e (m_h) the electron (hole) effective mass. Introducing the center-of-mass coordinate $R = \frac{m_e r_e + m_h r_h}{m_e + m_h}$ and the difference coordinate $r = r_e - r_h$, the general solution becomes of separable form, $\psi(r_e, r_h) = \frac{e^{iK.R}}{\sqrt{V}}\varphi(r)$, where $\varphi(r)$ is the wave function for the relative motion. The corresponding Hamiltonian reads:[41]

$$H_r = E_g - \frac{\hbar^2}{2\mu}\Delta_r - \frac{e^2}{4\pi\varepsilon_{eff} r} \quad (2)$$

J. Phys. Chem. C, 2014, 118 (22), pp 11566–11572 DOI: 10.1021/jp503337a

The reduced mass is defined by $1/\mu = 1/m_e + 1/m_h$. For the relative electron-hole motion, the Hamiltonian (2) has two types of solutions. First, bound pair states of energy $E_n = E_g - \frac{Ry}{n^2}$ where $Ry = \frac{\mu e^4}{2\hbar^2(4\pi\varepsilon_{eff})^2}$ is the exciton Rydberg energy, and n the quantum number (n=1 for the 1S exciton ground state, n=2 for the 2S exciton state, …). The wavefunctions are products of spherical harmonics and Laguerre polynomials.[41] The second type of solutions, corresponds to a continuum of pair states having energies larger than the bandgap energy. Their wavefunctions are not simple planewaves but products of spherical harmonics and complex radial components related to confluent hypergeometric functions.[41] Even though electron and hole states correspond to propagative states, the motions are weakly correlated. For that reason, the absorption of the continuum of pair states above the bandgap is enhanced as compared to simple band-to-band transitions when the electron-hole interaction is neglected in equation (1). This enhancement is important in the context of solar cells, because carriers are generated by light over a large spectral region, especially above the bandgap. The optical absorption reads: [41]

$$I(\tilde{E})/I_0 = 4\sum_{n=1}^{\infty}\frac{\gamma/n^3}{\left(\tilde{E}+1/n^2\right)^2+\gamma^2} + \int_0^{\infty}\frac{d\tilde{E}'}{\pi}\frac{\gamma S(\tilde{E}')\sqrt{\tilde{E}'}}{\left(\tilde{E}-\tilde{E}'\right)^2+\gamma^2} \qquad (3)$$

$\tilde{E} = \frac{\hbar\omega - E_g}{Ry}$ is a reduced energy, γ a broadening factor that depends on the temperature and $S(\tilde{E}) = \frac{2\pi}{\sqrt{\tilde{E}}\left(1-e^{-2\pi/\sqrt{\tilde{E}}}\right)}$ the absorption enhancement factor of the continuum of pair states. In the limit of free carriers or a totally screened interaction, the first sum (bound exciton pair states) disappears in equation (3) and $S(\tilde{E})$ reduces to 1. Simulated optical absorption spectra using

equation (3) are compared to experimental data in Figure 2 (see also Figure S5 in the Supporting Information) considering different dielectric constants to highlight screening effects. Experimental absorption spectra above the critical temperature Tc are well reproduced with a larger effective dielectric constant than below Tc. It yields a reduction of the 1S exciton binding energy for all the spectra above Tc, from *ca* 15 to 5meV (Figure 3). The value of the exciton binding energy being much smaller than kT (~26meV) at room temperature, we may infer that most electron-hole pairs are ionized yielding free carriers. This also leads to *ca* 80meV shift of the electronic bandgap at Tc (Figure 3).

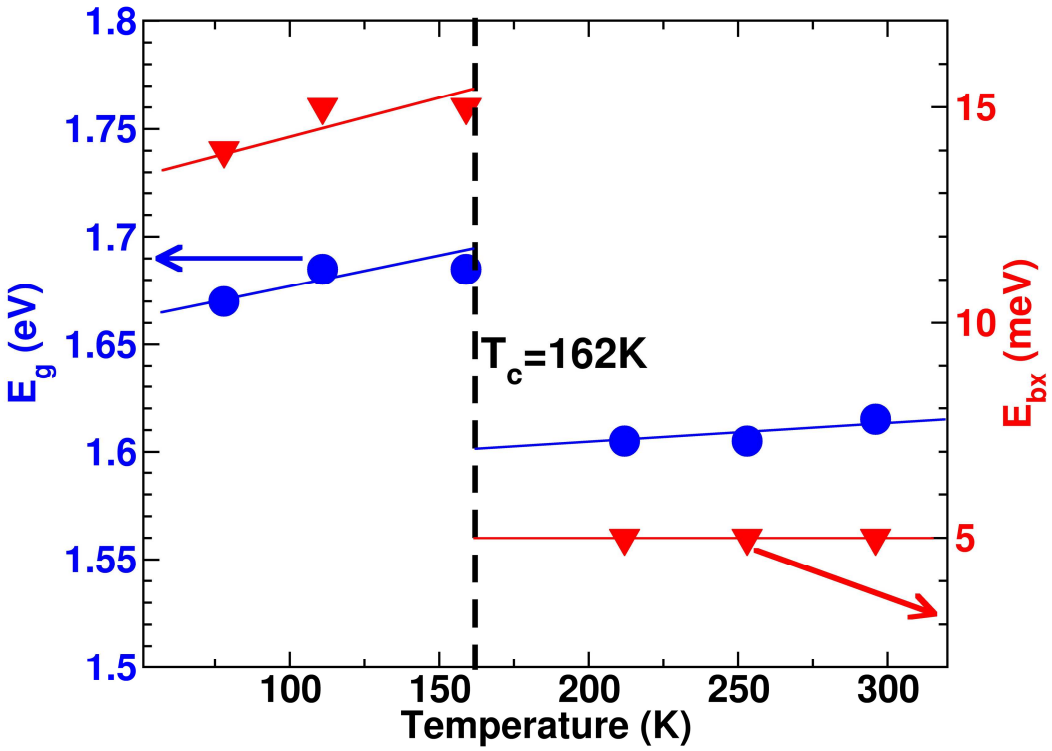

Figure 3. Electronic bandgap (left-hand axis) and exciton binding (right-hand axis) energies calculated from the experimental absorption spectra of $CH_3NH_3PbI_3$[27] using equation (3) for the computed absorption spectra (Figures 2 and S5 in the Supporting Information). Structural phase transition occurs at Tc=162K (black dashed line).

J. Phys. Chem. C, 2014, 118 (22), pp 11566–11572 DOI: 10.1021/jp503337a

This prompts a comment (see also in the Supporting Information) on exciton binding energies of 37-50 meV deduced from magnetoabsorption spectroscopy measurements at liquid helium temperature.[26,37] These values have been obtained considering the above mentioned Wannier exciton model, with an additional contribution related to magnetic coupling. As quoted by the authors, "*the only unknown parameter is the dielectric constant*" ε_{eff}.[26] The choice for the high frequency dielectric constant (6.5 for $CH_3NH_3PbI_3$) was motivated by the fact that "*the binding energy… is much larger than energies of optical phonon modes*".[26] However, from recent Raman scattering experiments, we know that this argument is not valid since optical phonons with energies as low as 8 meV (vibration of the inorganic cage) and 16 meV (libration of the organic cation) have been evidenced.[42] This suggest that the effective dielectric constant is most probably larger due to screening induced by vibrations at low temperature. Taking $\varepsilon_{eff} = 11$ as in Figure 2, the 1S exciton binding energy drops from 37-50 meV to 18-24 meV at 5K. The latter binding energies become close to those shown Figure 3. Moreover, no 2S exciton peak was reported in the experimental spectra at liquid helium temperature.[26,37] But, within the Wannier exciton model, equation (3), the 2S binding energy and intensity are $Ry/4$ and 8 times smaller, respectively. Thus, the 1S-2S splitting should amount to 37 and 57 meV for $CH_3NH_3PbI_3$ and $CH_3NH_3PbBr_3$, respectively. Given the experimental resolution and spectral broadening, the 2S state should have been detected.[26,27,37] This is also an indication that the 1S exciton binding energy was most probably overestimated.

The influence of the low temperature structural transition on the dielectric properties can be further investigated by reviewing the available data for $CH_3NH_3PbI_3$ and $CH_3NH_3PbCl_3$, summarized in Table S6 (Supporting Information, including additional discussion). These data evidence different features for the high and low frequency regimes as sketched Figure 4. First,

J. Phys. Chem. C, 2014, 118 (22), pp 11566–11572 DOI: 10.1021/jp503337a

the high frequency behavior can be related to vibrational polar phonons of the lattice by analogy with reflectivity measurements on the all-inorganic analogue $CsPbCl_3$.[43] From comparison of dielectric measurements at 1KHz[29] and millimeter wave spectroscopy at 90GHz,[28] we conclude that the high frequency vibrational contributions are little affected by the phase transition in $CH_3NH_3PbX_3$. Next, an additional contribution shows up above Tc in the low frequency range (Figure 4). We attribute this dielectric increment to the collective tumbling of cation's C-N axis at RT, evidenced by NMR[30], dielectric[29] and millimeter wave spectroscopies.[28] A similar drop in the dielectric spectra of alkali-cyanides has been reported and related to the collective tumbling of C-N- anions that get frozen in the LT phase.[44] In C_{60} fullerenes, the self-localized exciton observed at LT becomes a diffusing free exciton above a critical temperature where free rotations of C_{60} molecules are collectively activated.[45] In $C_5H_{10}NH_2PbI_3$, a 1D hybrid perovskite, strongly bound excitons are formed, the exciton being self-trapped by deforming the lattice in its neighbourhood,[46] but with a clear Stokes shift (1.2eV) which is not observed in 3D compounds like $CH_3NH_3PbI_3$. It is worth mentioning that among the all-inorganic perovskites $CsPbX_3$, $CsPbI_3$ is the only one exhibiting a self-trapped exciton at LT with a sizeable Stokes shift (0.74eV).[47] In addition, our simulated absorption spectra around T_c (Figure 2) and our analysis of liquid helium experimental results, indicate that the effective dielectric constant is somewhat larger than its high frequency limit ($\varepsilon_\infty \approx 6.5$) below Tc, suggesting possible exciton screening by polar modes. For $CH_3NH_3PbX_3$, we can thus conclude that the LT exciton resonance is related to a Wannier like exciton already partially screened by polar modes, that becomes completely screened above Tc, yielding almost free carriers when the orientational motions of the cations are collectively activated by a structural phase transition.

J. Phys. Chem. C, 2014, 118 (22), pp 11566–11572 DOI: 10.1021/jp503337a

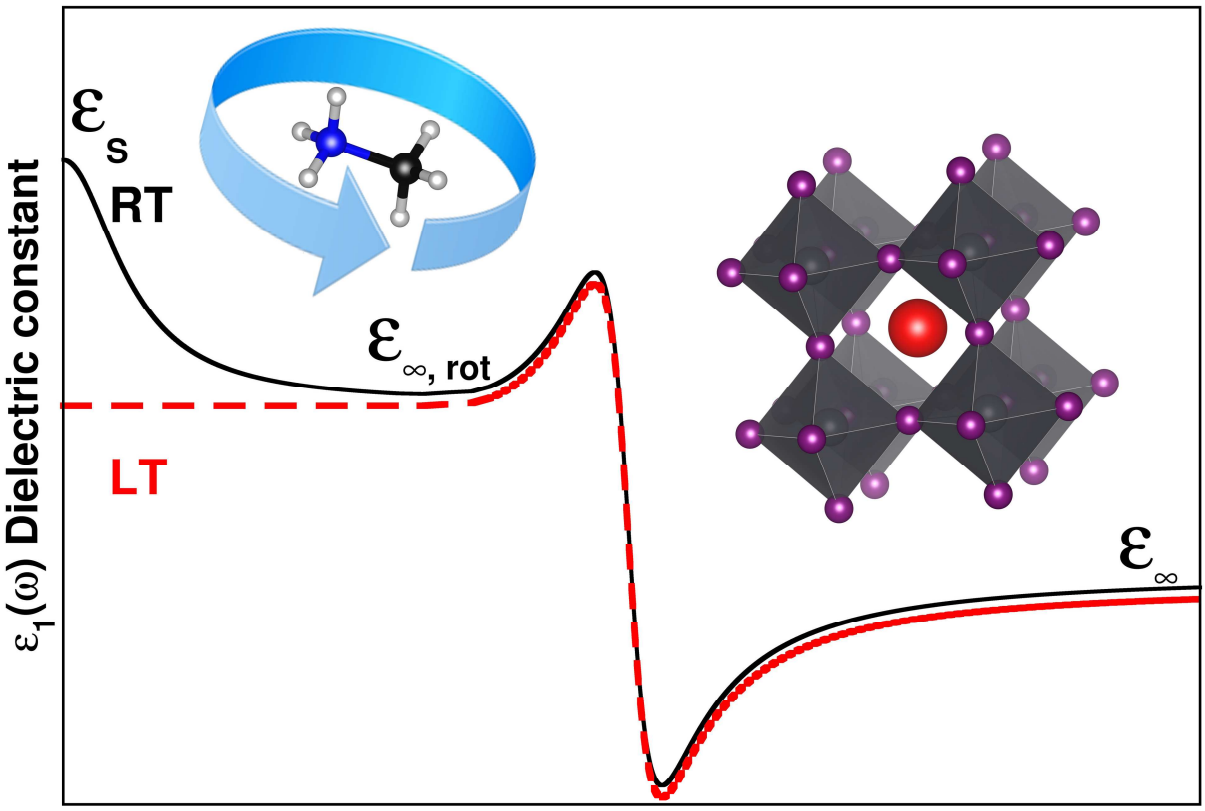

Figure 4. Schematic drawing of the dielectric constant as a function of frequency displaying respective contributions of $CH_3NH_3^+$ rotations and perovskite's vibrational phonons. Frequency dependence of the dielectric constant of $CH_3NH_3PbX_3$ as derived from available experimental data summarized in Table S6 (Supporting Information). The high frequency response is related to vibrational polar phonons stemming from modes of the perovskite lattice (right-hand side). The low frequency region (left-hand side) shows significant differences for the low (LT, red dash line) and room (RT, black line) temperature phases. The static dielectric constant (ε_S) increase at RT is primarily attributed to rotational motion of $CH_3NH_3^+$ cations.

In the cubic $CH_3NH_3PbX_3$ hybrid perovskites, each $CH_3NH_3^+$ cation is located in a cuboctahedral cage formed by the 12 nearest halogen atoms. The size of this cage reduces when

iodine is substituted by chlorine (-25%), leading to restricted molecular motion.[28] Thus, the drop in dielectric constant is larger for iodine-based compounds. It shows up in different Lorentz local field factors evidencing the different dielectric environments in both compounds.[28] A similar variation of cell volume is observed between KCN and NaCN crystals, with a smaller cell for the latter,[48] leading to a glassy disorder for CN- ions and local strain in mixed crystals. The different behavior of the reorientation dynamics of CN- between these two alkali-cyanides has been attributed to both the smaller size of the NaCN lattice and to reduced polarizability for Na^+ as compared to K^+. Moreover, it has been shown that the CN^- collective ordering is severely affected by insertion of alkali metals of another size. The cationic impurities strongly hinder rotation of CN^- ions that are prevented to take part in the collective process. We propose in this work that a comparable effect appears upon halogen doping in 3D hybrid perovskites. If collective tumbling of $CH_3NH_3^+$ is hampered, exciton screening will be reduced leading to a sizeable increase in absorption. Such enhancement of absorption upon Cl doping has been evidenced in $CH_3NH_3PbI_3$[21,24] and $CH_3NH_3PbBr_3$.[49] Further studies at low temperature by time-resolved photoluminescence, pump-probe experiments or dielectric measurements should allow to confirm this point.

Molecular motions that affect electron-hole interactions is also expected to change the drift-diffusion current for electrons and holes. At high temperature (T>Tc), tumbling of $CH_3NH_3^+$ cations may couple to carrier mobility in the perovskite crystal. Indeed, at RT current-voltage characteristics of $CH_3NH_3PbI_3$ exhibit a ferroelectric hysteresis attributed to the reorientation of the permanent dipoles of $CH_3NH_3^+$ on application of an external electric field in addition to the resistance of the inorganic lattice.[31] Polarization measurements and analysis of the coercive field in the current-voltage hysteresis loops are also in favor of charge motion within the material.[31]

J. Phys. Chem. C, 2014, 118 (22), pp 11566–11572 DOI: 10.1021/jp503337a

Chlorine doping might restrict collective rotations of the $CH_3NH_3^+$ and consequently increase electron-hole diffusion lengths for $CH_3NH_3PbI_{3-x}Cl_x$ as compared to $CH_3NH_3PbI_3$. Such interpretation is consistent with experimental findings.[14,24] The morphology of hybrid perovskite grains is also important for transport properties. Intergranular barriers, rather than intrinsic mechanisms probably dominate carrier transport in highly disordered samples and different grain sizes may result from alloys in such compounds. However, in high quality samples substantial charge carrier mobility losses at grain boundaries do not prevail.[24]

In summary, this work indicates that the broad light-harvesting abilities of the inorganic-organic family of perovskites $CH_3NH_3MX_3$, recently used for high-performance solar cells, is a direct consequence of their multi-bandgap and multi-valley nature. In some sense, they can be thought as natural multi-junction. The low energy absorption peak at 760nm in $CH_3NH_3PbI_3$ is attributed to the direct bandgap transition at the high-symmetry point R from the VB maximum to CB minimum. The peak located at 480nm corresponds mainly to a direct transition at M, with additional contributions from secondary direct transitions at R. Moreover, the carriers redistribution after optical excitation is facilitated by a channel from R to M. Inspection of the dielectric responses over a wide frequency range allows clarifying the nature of the photoexcited species created in these materials. In particular, as shown in this work, the Wannier-like exciton evidenced at low temperature becomes almost entirely screened at room temperature, yielding free carriers, due to optical phonons and collective rotational motion of the organic cations. In mixed-halides perovskites, the insertion of a halide of another size is suggested to prevent such collective reorientations, thus reducing exciton screening and enhancing optical absorption. This picture is also consistent with the counterintuitive increase of carrier mobility experimentally evidenced upon doping.[14,24] In fact, the local lattice disorder brought by alloying should reduce

J. Phys. Chem. C, 2014, 118 (22), pp 11566–11572 DOI: 10.1021/jp503337a

electron-hole diffusion lengths. But, doping might restrict molecular motion and enhance transport properties. Low temperature time-resolved photoluminescence, pump-probe experiments should be able to confirm the impact of the phase transition on the exciton screening. Dielectric measurements on mixed lead-halide perovskites may also help to clarify the role of halide doping on the collective rotational motion.

Corresponding Author

*Email: Jacky.Even@insa-rennes.fr, Claudine.Katan@univ-rennes1.fr

Notes

The authors declare no competing financial interests.

Acknowledgments

This work was performed using HPC resources from GENCI-CINES/IDRIS grant 2013-c2012096724. The work is supported by Agence Nationale pour la Recherche (PEROCAI project ANR-10-04).

Supporting Information Available:

Computational details, additional details and discussions for theoretical models, electronic band structures, absorption spectra, gap (exciton) switching and dielectric properties. This material is available free of charge via the Internet at http://pubs.acs.org.

J. Phys. Chem. C, 2014, 118 (22), pp 11566–11572 DOI: 10.1021/jp503337a

REFERENCES

(1) Shockley, W.; Queisser, H. J. Detailed balance limit of efficiency of p-n junction solar cells. *J. Appl. Phys.* **1961**, *32*, 510-519.

(2) Green, M. A.; Emery, K.; Hishikawa, Y.; Warta, W.; Dunlop, E.D. Solar cell efficiency tables (version 42). *Prog. Photovolt: Res. Appl.* **2013**, *21*, 827–837.

(3) Friedman, D.J. Progress and challenges for next-generation high-efficiency multijunction solar cells, *Current Opinion in Solid State and Materials Science* **2010**, *14*, 131-138.

(4) Kojima, A.; Teshima, K.; Shirai, Y.; Miyasaka T. Organometal halide perovskites as visible-light sensitizers for photovoltaic cells. *J. Am. Chem. Soc.* **2009**, *131*, 6050-6051.

(5) Lee, M. M.; Teuscher, J.; Miyasaka, T.; Murakami, T. N.; Snaith, H. J. Efficient hybrid solar cells based on meso-superstructured organometal halide perovskites. *Science*. **2012**, *338*, 643-647.

(6) Kim, H-S.; Lee, C. R.; Im, J. H.; Lee, K. B.; Moehl, T.; Marchioro, A.; Moon, S. J.; Humphry-Baker, R.; Yum, J. H.; Moser, J. E.; Grätzel, M.; Park, N. G.. Lead iodide perovskite sensitized all-solid-state submicron thin film mesoscopic solar cell with efficiency exceeding 9%. *Sci. Rep.* **2012**, *2*, 591-1-591-7.

(7) Heo, J. H.; Im, S. H.; Noh, J. H.; Mandal, T. N.; Lim, C. S.; Chang, J. A.; Lee, Y. H.; Kim, H. J.; Sarkar, A.; Nazeeruddin, Md. K.; Grätzel, M.; Seok, S. II. Efficient inorganic–organic hybrid heterojunction solar cells containing perovskite compound and polymeric hole conductors. *Nature Photonics*. **2013**, *7*, 486-491.

(8) Burschka, J; Pellet, N.; Moon, S. J.; Humphry-Baker, R.; Gao, P.; Nazeeruddin, M. K.; Grätzel, M.. Sequential deposition as a route to high-performance perovskite-sensitized solar cells. *Nature*. **2013**, *499*, 316-319.

(9) Kim, H.-S; Mora-Sero, I.; Gonzalez-Pedro, V.; Fabregat-Santiago, F.; Juarez-Perez, E. J.; Park, N. G.; Bisquert, J. Mechanism of carrier accumulation in perovskite thin-absorber solar cells. *Nature Comm*. **2013**, *4*, 2242.

(10) Park, N. G. Organometal perovskite light absorbers toward a 20% efficiency low-cost solid-state mesoscopic solar cell. *J. Phys Chem. Lett*. **2013**, *4*, 2423-2429.

(11) Noh, J. H.; Im, S. H.; Heo, J. H.; Mandal, T. N.; Seok, S. I. Chemical management for colorful, efficient, and stable inorganic–organic hybrid nanostructured solar cells. *Nano Lett*. **2013**, *13*, 1764-1769.

(12) Liu, M.; Johnston, M. B.; Snaith, H. J. Efficient planar heterojunction perovskite solar cells by vapour deposition. *Nature*. **2013**, *501*, 395-398.

(13) Snaith, H. J. Perovskites: The emergence of a new era for low-cost, high-efficiency solar cells. *J. Phys Chem. Lett*. **2013**, *4*, 3623-3630.

(14) Stranks, S. D.; Eperon, G. E.; Grancini, G.; Menelaou, C.; Alcocer, M. J. P.; Leijtens, T.; Herz, L. M.; Petrozza, A.; Snaith, H. J. Electron-hole diffusion lengths exceeding 1 micrometer in an organometal trihalide perovskite absorber. *Science*. **2013**, *342*, 341-344.

(15) Xing, G; Mathews, N.; Sun, S.; Lim, S. S.; Lam, Y. M.; Grätzel, M.; Mhaisalkar, S.; Sum, T. C. Long-range balanced electron- and hole-transport lengths in organic-inorganic $CH_3NH_3PbI_3$. *Science*. **2013**, *342*, 344-347.

(16) Loi, M. A.; Hummelen, J. C. Hybrid solar cells: Perovskites under the sun. *Nature Mater*. **2013**, *12*, 1087-1089.

J. Phys. Chem. C, 2014, 118 (22), pp 11566–11572 DOI: 10.1021/jp503337a

(17) Even, J.; Pedesseau, L.; Jancu, J.-M.; Katan, C. Importance of spin–orbit coupling in hybrid organic/inorganic perovskites for photovoltaic applications. *J. Phys. Chem. Lett.* **2013**, *4*, 2999-3005.

(18) Even, J.; Pedesseau, L.; Jancu, J.-M.; Katan, C. DFT and k • p modelling of the phase transitions of lead and tin halide perovskites for photovoltaic cells. *Phys. Status Solidi RRL*. **2014**, *8*, 31–35.

(19) Brivio, F.; Walker, A. B.; Walsh, A. Structural and electronic properties of hybrid perovskites for high-efficiency thin-film photovoltaics from first-principles. *Appl. Phys. Lett. Mat.* **2013**, *1*, 042111-1-042111-5.

(20) Baikie, T.; Fang, Y.; Kadro, J. M.; Schreyer, M.; Wei, F.; Mhaisalkar, S. G.; Graetzel, M.; White, T. J. Synthesis and crystal chemistry of the hybrid perovskite $(CH_3NH_3)PbI_3$ for solid-state sensitised solar cell applications. *J. Mater. Chem. A*. **2013**, *1*, 5628-5641.

(21) Colella, S.; Mosconi, E.; Fedeli, P.; Listorti, A.; Gazza, F.; Orlandi, F.; Ferro, P.; Besagni, T.; Rizzo, A.; Calestani, G.; Gigli, G.; De Angelis, F.; Mosca, R. $MAPbI_{3-x}Cl_x$ mixed halide perovskite for hybrid solar cells: The role of chloride as dopant on the transport and structural properties. *Chem. Mater*. **2013**, *25*, 4613-4618.

(22) Mosconi, E.; Amat, A.; Nazeeruddin, Md. K.; Grätzel, M.; De Angelis, F. First-principles modeling of mixed halide organometal perovskites for photovoltaic applications. *J. Phys. Chem. C* **2013**, *117*, 13902-13913.

(23) Giorgi, V.; Fujisawa, J.-I.; Segawa, H.; Yamashita, K. Small photocarrier effective masses featuring ambipolar transport in methylammonium lead iodide perovskite: A density functional analysis. *J. Phys. Chem. Lett.* **2013**, *4*, 4213-4216.

J. Phys. Chem. C, 2014, 118 (22), pp 11566–11572 DOI: 10.1021/jp503337a

(24) Wehrenfennig, C.; Eperon, G. E.; Johnston, M. B.; Snaith, H. J.; Herz, L. M. High charge carrier mobilities and lifetimes in organolead trihalide perovskites. *Adv. Mat.* **2014** *26*, 1584-1589.

(25) Kim, H.S.; Im, S. H.; Park, N.-G. Organolead Halide Perovskite: New Horizons in Solar Cell Research. *J. Phys. Chem. C* **2014**, DOI: 10.1021/jp409025w

(26) Hirasawa, M.; Ishihara, T.; Goto, T.; Uchida, K.; Miura, N. Magnetoabsorption of the lowest exciton in perovskite-type compound (CH_3NH_3)PbI_3. Physica B. 1994, 201, 427-430.

(27) Ishihara, T. Optical properties of PbI-based perovskite structures, *J. of Lum.* **1994**, *60&61*, 269-274.

(28) Poglitsch, A.; Weber, D. Dynamic disorder in methylammoniumtrihalogenoplumbates (II) observed by millimeter-wave spectroscopy. *J. Chem. Phys.* **1987**, *87*, 6373-6378.

(29) Onoda-Yamamuro, N.; Matsuo, T.; Suga, H., Dielectric study of $CH_3NH_3PbX_3$ (X = Cl, Br, I). *J. Phys. Chem. Solids* **1992**, *53*, 935-939.

(30) Wasylishen, R. E.; Knop, O.; Macdonald, J. B., Cation rotation in methylammoniumlead halides. *Solid State Comm.* **1985**, *56*, 581-582.

(31) Stoumpos, C. C.; Malliakas, C. D.; Kanatzidis, M. G. Semiconducting tin and lead iodide perovskites with organic cations: Phase transitions, high mobilities, and near-infrared photoluminescent properties. *Inorg. Chem.* **2013**, *52*, 9019-9038.

(32) Even, J.; Pedesseau, L.; Dupertuis, M.-A.; Jancu, J.-M.; Katan, C. Electronic model for self-assembled hybrid organic/perovskite semiconductors: Reverse band edge

electronic states ordering and spin-orbit coupling. *Phys. Rev. B*. **2012**, *86*, 205301-1-205301-4.

(33) Ferreira, R.; Bastard, G. Phonon-assisted capture and intradot Auger relaxation in quantum dots. *Appl. Phys. Lett*. **1999**, *74*, 2818-2820.

(34) Ohnesorge, B.; Albrecht, M.; Oshinowo, J.; Forchel, A.; Arakawa, Y. Rapid carrier relaxation in self-assembled InxGa1-xAs/GaAs quantum dots. *Phys. Rev. B* **1996,** *54*, 11532-11538.

(35) Miska, P.; Even, J.; Marie, X.; Dehaese, O. Electronic structure and carrier dynamics in InAs/InP double-cap quantum dots. *Appl. Phys. Lett*. **2009**, *94*, 061916-1-061916-3.

(36) Kitazawa, N.; Watanabe, Y.; Nakamura, Y. Optical properties of $CH_3NH_3PbX_3$ (X = halogen) and their mixed-halide crystals. *J. Mat. Sci*. **2002**, *37*, 3585-3587.

(37) Tanaka, K.; Takahashi, T.; Ban, T.; Kondo, T.; Uchida, K.; Miura, N. Comparative Study on the Excitons in Lead-Halide-Based Perovskite-Type Crystals $CH_3NH_3PbBr_3$ $CH_3NH_3PbI_3$. Solid State Commun. **2003**, *127* (9–10), 619–623.

(38) Edri, E.; Kirmayer, S.; Mukhopadhyay, S.;,Gartsman, K.; Hodes, G.; Cahen, D. Elucidating the charge carrier separation and working mechanism of $CH_3NH_3PbI_{3-x}Cl_x$ perovskite solar cells. *Nature Comm*. **2014**, DOI: 10.1038/ncomms4461

(39) Xing, G.; Mathews, S.; Lim, S. S.; Yantara, N.; Liu, X.; Sabba, D.; Grätzel, M.; Mhaisalkar, S.; Sum, T.C.; Low-temperature solution-processed wavelength-tunable perovskites for lasing. *Nature Mater*. **2014**, DOI: 10.1038/NMAT3911

(40) Pedesseau, L.; Jancu, J-M.; Rolland, A.; Deleporte, E.; Katan, C.; Even, J. Electronic properties of 2D and 3D hybrid organic/inorganic perovskites for

optoelectronic and photovoltaic applications. *Opt. Quant. Electron.* **2013**, DOI: 10.1007/s11082-013-9823-9

(41) Chuang, S. Physics of Optoelectronic Devices. (J. W. Goodman Ed., New York: Wiley, **1995**).

(42) Quarti, C.; Grancini, G.; Mosconi, E.; Bruno, P.; Ball, J. M.; Lee, M. M.; Snaith, H. J.; Petrozza, A.; De Angelis, F. The Raman Spectrum of the $CH_3NH_3PbI_3$Hybrid Perovskite: Interplay of Theory and Experiment. J. Phys. Chem. Lett. **2014**, *5*, 279–284

(43) Hirotsu, S. Far-infrared reflectivity specra of $CsPbCl_3$. *Phys. Lett. A* **1972**, *41*, 55-56.

(44) Ortiz-Lopez, J. Dipolar Reorientation and Order-Disorder Behavior of Pure and Mixed Alkali Cyanides. *Phys. Rev. Lett.* **1983**, *50*, 1289–1292.

(45) Matus, M.; Kuzmany, H.; Sohmen, E. Self-Trapped Polaron Exciton in Neutral Fullerene C_{60}. *Phys. Rev. Lett.* **1992**, *68*, 2822-2825.

(46) Nagami, A.; Okamura, K.; Ishihara, T. Optical properties of a quantum wire crystal, $C_5H_{10}NH_2PbI_3$. *Physica B* **1996**, *227*, 346-348.

(47) Nikl, M.; Nitsch, K.; Chval, J.; Somma, F.; Phani, A. R.; Santucci, S.; Giampaolo, C.; Fabeni, P.; Pazzi, G. P.; Feng, X. Q. Optical and structural properties of ternary nanoaggregates in CsI–PbI_2 co-evaporated thin films. *J. Phys.: Condens. Matter*. **2000**, *12*, 1939–1946.

(48) Ortiz-Lopez, J.; Lüty, F. Dielectric Studies of CN– Dipolar Reorientation and Order–Disorder Behavior in $RbCN_{1-x}$:KCN_x and KCN_{1-x}:$NaCN_x$. *Phys. status solidi (b)* **2001**, *228*, 893–917.

J. Phys. Chem. C, 2014, 118 (22), pp 11566–11572 DOI: 10.1021/jp503337a

(49) Edri, E.; Kirmayer, S.; Kulbak, M.; Hodes, G.; Cahen, D. Chloride Inclusion and Hole Transport Material Doping to Improve Methyl Ammonium Lead Bromide Perovskite-Based High Open-Circuit Voltage Solar Cells. *J. Phys. Chem. Lett.* **2014**, *5*, 429-433.